RSC Advances

PAPER

View Article Online
View Journal | View Issue

Cite this: *RSC Adv.*, 2026, **16**, 6865

Topology-enhanced oil adsorption by flower-like mesoporous silica nanoparticles for advanced cosmetic oil control

Minjia Yuan,[ab] Zhihui Zheng,[b] Yan Yu,[a] Yi Wang,[a] Wenxing Wang, *[a] Qi Li,[b] Xiaomin Li *[a] and Dongyuan Zhao *[a]

Received 6th November 2025
Accepted 26th January 2026

DOI: 10.1039/d5ra08525j

rsc.li/rsc-advances

To address the growing demand for advanced oil-control materials in cosmetics, this study developed novel flower-like mesoporous silica nanoparticles (FLS) with topology-enhanced oil–adsorption properties. Using a biphasic microemulsion synthesis strategy, FLS with petal-like surface topology, radial pore channels, and excellent colloidal stability were successfully prepared. Compared with conventional mesoporous silica nanoparticles (MSN) with small mesopores (2–3 nm) synthesized *via* the classical Stöber method, FLS exhibited significantly superior oil-absorption capacity across a wide range of oils, with maximum uptake nearly twice that of MSN. Notably, FLS showed exceptional adsorption efficiency for large-molecular-weight oils, demonstrating an approximately 226.3% increase over MSN in adsorbing PDMS-15000 w. This remarkable enhancement is attributed to the unique flower-like topology, which provides large open concave structures for instantaneous oil wetting and straight, radially aligned mesochannels for rapid oil transport and maximized pore utilization. *In vivo* human skin tests further confirmed the cosmetic efficacy of FLS. Collectively, these findings position FLS as a next-generation oil-control material and highlight topology-enhanced oil adsorption as a novel design strategy for advanced adsorbents.

1 Introduction

Porous materials have been widely applied across diverse scientific and technological fields due to their high specific surface area, interconnected porosity, low density, and exceptional adsorption capabilities endowed by their unique network structures and pore characteristics.[1–5] According to the International Union of Pure and Applied Chemistry (IUPAC) classification, porous materials can be categorized into three categories based on pore size: microporous (pore diameter < 2 nm), mesoporous (2 nm ≤ pore diameter ≤ 50 nm), and macroporous (pore diameter > 50 nm).[6–8] Among these, mesoporous materials uniquely combine the high specific surface area property of microporous materials and the enhanced mass- and energy-transfer efficiencies of macroporous materials, exhibiting outstanding performance in diverse applications such as adsorption, loading, and confined reactions.[9–11] As a key member of the mesoporous materials family, mesoporous silica nanomaterials have achieved substantial advances in structural design, scalable synthesis, and performance optimization.[12–15] Decades of research on mesoporous silica nanomaterials have established comprehensive methodologies enabling precise control over critical properties including particle size, pore architecture, and morphology.[16–18] Based on these properties, mesoporous silica nanomaterials show broad application prospects in versatile fields such as energy, catalysis, drug delivery and advanced cosmetic formulations.[19,20]

In the cosmetics field, developing oil control products to address the issues associated with oily skin and its accompanying skin problems (such as facial shine, enlarged pores, dull complexion, acne, seborrheic dermatitis, *etc.*) has always been a major focus.[21–23] Rapid physical adsorption of excess sebum from the skin surface is the predominant strategy for effective oil-control in cosmetic formulations.[24,25] Current oil-absorbing ingredients for oil control products fall into three categories: inorganic powders (*e.g.*, silica, talc), organic powders (*e.g.*, PMMA, silicone elastomer microspheres), and natural powders (*e.g.*, corn starch, tapioca starch).[26–28] However, the adsorption performance of existing cosmetic-grade oil-absorbing materials remains suboptimal, driving a persistent need for the development of novel adsorbents. Recently, mesoporous silica nanomaterials, with inherent high porosity, large specific surface area and high biocompatibility, are recognized as promising candidates for highly efficient oil adsorption.[29–31] Many studies have demonstrated the great promise of mesoporous silica nanomaterials in developing next-generation oil control products.[32,33] However,

[a]*Department of Chemistry, Laboratory of Advanced Materials, Shanghai Key Laboratory of Molecular Catalysis and Innovative Materials, State Key Laboratory of Molecular Engineering of Polymers, Fudan University, Shanghai, China. E-mail: wangwenxing@fudan.edu.cn; lixm@fudan.edu.cn; dyzhao@fudan.edu.cn*
[b]*Shanghai Qiran Biotechnology Co., Ltd, Shanghai 201702, China*

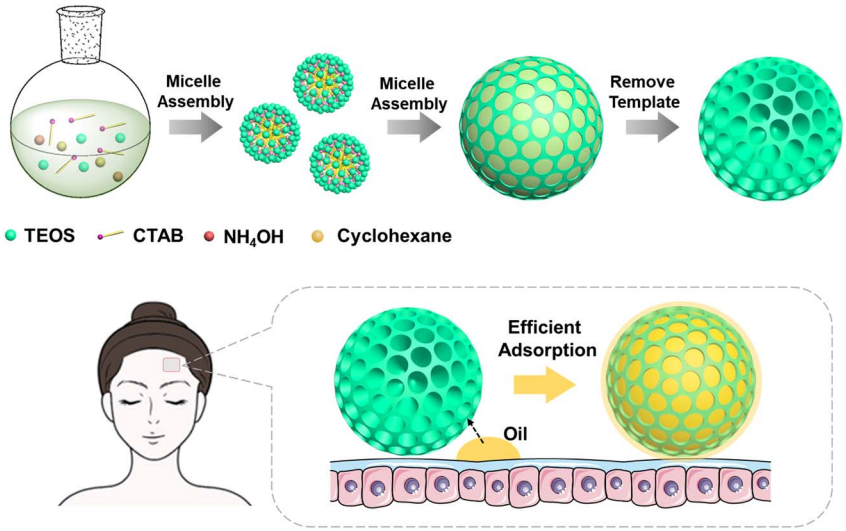

Fig. 1 Schematic illustration of the synthesis and oil-control application of FLS.

despite the utilization of mesoporous silica nanomaterials in oil control products, fundamental understanding of structure–adsorption relationships in mesoporous silica applications remains limited. To date, existing studies predominantly focus on properties like specific surface area or surface hydrophobicity,[34,35] while the critical influence of pore geometry remains unexplored. Elucidating how pore architecture governs adsorption performance would provide crucial insights to unlock the full potential of mesoporous silica nanomaterials for advanced formulations that enhance skin health and appearance.

Herein, we have developed a novel flower-like mesoporous silica nanoparticles (FLS) for superior oil control and revealed a topology-mediated mechanism underlying their enhanced oil adsorption capacity (Fig. 1). The FLS featuring a petal-like surface topology and radial pore architecture with excellent colloidal stability was successfully fabricated *via* a bi-phase microemulsion method and its pore geometry and surface topology was well preserved after calcination. The nitrogen-sorption and Brunauer–Emmett–Teller (BET) analysis determines that FLS has a specific surface area of ~256 $m^2 g^{-1}$, a pore size of ~24.4 nm and a large pore volume of ~1.12 $cm^3 g^{-1}$. Compared to conventional mesoporous silica nanomaterials (MSN) synthesized by the classical Stöber method, either with comparable specific surface area (~271 $m^2 g^{-1}$, MSN-271) or much higher specific surface area (~504 $m^2 g^{-1}$, MSN-504), FLS possesses superior oil absorption capacity, which is about twice that of MSN-271 and ~1.5 times that of MSN-504 across ten commonly used test oils. Importantly, FLS showed exceptional adsorption toward large-molecule oils, with an uptake of 1.86 mL g^{-1} for PDMS-15 000 w, representing a 226.3% increase compared with MSN-504. Further investigations revealed a topology-mediated oil adsorption mechanism for the superior oil adsorption capacity of FLS. Contact angle measurements show that FLS possesses the similar hydrophilic surface to MSN but exhibits significantly faster wetting kinetics, indicating that the arranged petal-like structures on the surface of FLS plays a key role in accelerating oil penetration. Furthermore, oil immersion tests show that FLS is able to accommodate more oil molecules than MSN, underscoring the critical role of pore nanoarchitecture in maximizing pore space utilization for oil adsorption. Collectively, these findings indicate that the flower-like topology enhances oil adsorption through two synergistic effects: (1) the radially arranged nano-petals on the surface of FLS create large surface concavities, thus provide highly accessible entrance for instantaneous oil penetration; (2) the radially oriented mesoporous channels inside the FLS provide straight pathways for oil transport, thereby maximizing the pore volume occupancy. Based on its outstanding exceptional oil adsorption capability, FLS was incorporated into test cream exhibited a dose-dependent sebum-control effect *in vivo* on human skin. Remarkably, an addition of only 0.3 wt% FLS achieved effective sebum adsorption performance with efficacy lasting up to 4 hours. Comparative studies with conventional MSN and the commonly used commercial silica (CS) further confirmed the superior sebum adsorption performance of FLS.

2 Experimental section

2.1 Chemicals and materials

Hexadecyltrimethylammonium bromide (CTAB) were purchased from Sigma-Aldrich. Cyclohexane, ammonia aqueous solution (28 wt%), urea and ethanol (99.8%) were obtained from Shanghai Chemical Co., Ltd. Tetraethyl orthosilicate (TEOS) were purchased from Aladdin Reagent Co., Ltd. Dibutyl phthalate, tridecyl trimellitate, dicaprylyl carbonate, caprylic/capric triglyceride, Jojoba seed oil, squalane, dimethicone, cyclopentasiloxane and diisostearyl malate were purchased from Aladdin Reagent Co., Ltd. Silica 150H was purchased from Sunjin Beauty Science Co., Ltd.

2.2 Synthesis of flower-like mesoporous silica spherical nanoparticles (FLS)

The flower-like mesoporous silica spheres (FLS) were synthesized *via* a bi-phase microemulsion method.[36] Briefly, a stable

microemulsion was first formed by adding 82 wt% deionized water, 1.8 wt% cetyltrimethylammonium bromide (CTAB), 7.0 wt% cyclohexane, and 1.5 wt% ammonium hydroxide (NH_4OH) into a flask. The mixture was heated to 70 °C and stirred for 2 hours to obtain a homogeneous system. Then, 4.0 wt% tetraethyl orthosilicate (TEOS) and 4.7 wt% urea was injected stepwise at a rate of 0.5 mL min^{-1}. The reaction was maintained at 70 °C with continuous stirring to trigger the urea decomposition, which then led to increased pH in this system and drove hydrolysis and condensation of TEOS at the micellar interface. After a reaction for 6 h, the FLS product was separated by centrifugation (9000 rpm, 10 min) and washed sequentially three times with an ethanol/water mixture (V/V = 1 : 1) and pure ethanol. The precursor was then dried at 60 °C for 12 hours, followed by template removal through calcination in a tube furnace at 550 °C for 6 hours in air with a heating rate of 2 °C min^{-1}. And the FLS product with radial mesoporous channels was finally obtained and ready for subsequent characterizations and tests.

2.3 Synthesis of conventional MSN based on the classical Stöber method

The conventional MSN with different surface areas were synthesis based on the classical Stöber method.[37] Typically, for the synthesis of MSN-271, 82 wt% deionized water, 0.5 wt% CTAB, and 1.5 wt% NH_4OH were added to a flask. The mixture was heated to 70 °C and stirred for 2 h to form a stable and clear micellar solution. The subsequent steps were identical to those for FLS synthesis.

For the synthesis of MSN-504, 82 wt% deionized water, 1.8 wt% CTAB, 0.5 wt% cyclohexane, and 1.5 wt% NH_4OH were added to a flask. The mixture was heated to 70 °C and stirred for 2 h to form a stable microemulsion. The subsequent steps were identical to those for FLS synthesis.

2.4 Measurements and characterization

Scanning electron microscopy (SEM) images were captured using field emission scanning electron microscopy (FESEM, Hitachi S-4800, Japan). Transmission electron microscopy (TEM) images were acquired on JEM-2100F transmission electron microscope with an accelerating voltage of 200 kV. Energy-dispersive X-ray spectroscopy (EDS) element mapping were conducted on a JEM-2100F EDX instrument. Nitrogen adsorption–desorption measurements were conducted at 77 K with ASAP 2420. Before measurements, the samples were degassed in vacuum at 180 °C for at least 12 h. The Brunauer–Emmett–Teller (BET) method was utilized to calculate the specific surface areas and the Barrett–Joyner–Halenda (BJH) model was utilized to calculate the pore volumes and the pore size distributions derived from the adsorption branches of isotherms. Fourier transform infrared (FTIR) spectra were recorded using Fourier transform infrared spectrometer (ThermoFisher, Nicolet iS10, USA). Dynamic light scattering (DLS) analysis and zeta-potential measurements were conducted on a Malvern ZS90 with a He, Ne laser (633 nm, 4 mW). The sample concentration used for the DLS measurements was 0.1 wt%.

2.5 Oil absorption test

The oil absorption value was determined according to the Chinese National Standard GB/T 3780.2 "Carbon Black – Part 2: determination of oil absorption value" using the following procedure: (1) the test material was ground, sieved, and dried at 125 °C for 12 hours, followed by cooling in a desiccator. (2) Test oil was continuously added from a microburette to a measured quantity of the dried material in a suitable container. (3) The mixture of material and oil was stirred until the formation of a cohesive paste, which could be rolled into a strand without leaving traces of oil. (4) The volume of oil consumed was recorded at this endpoint. The oil absorption value is expressed in mL per 100 grams of material (mL/100g). Each test was performed in triplicate to ensure data accuracy.

2.6 Human sebum adsorption experiment

The sebum adsorption capacity of FLS was characterized *via* a human oil-control experiment and the methodology referred to the Chinese Group Standard T/ZHCA 002-2018 "Test Method for Oil Control Efficacy of Cosmetics". The evaluation was conducted by comparing the changes in sebum content in the test areas applied with a blank cream (without FLS) and a test cream (with FLS), respectively. The Volunteers (n = 12 per group), aged between 18 and 55 years, participated after providing informed consent. The experimental steps are as follows: first, the volunteer's face was thoroughly cleansed using a soap-based cleanser and gently dried with lint-free absorbent paper. After a 30-minute acclimatization period under controlled conditions (20–22 °C and 40–60% relative humidity), baseline sebum content was measured on both the left and right sides of the forehead using a Sebumeter SM815. Then, the blank cream and the test cream were randomly applied to the left and right sides of the forehead, respectively, at a dosage of 2.0 ± 0.1 mg cm^{-2}. Sebum content was measured again at 0.5, 1.0, 2.0, and 4.0 hours post-application and calculated based on the baseline sebum content. The adsorption performance of FLS was characterized by the relative sebum adsorption change rate, calculated using the formula:

$$\text{Relative sebum adsorption rate}(\%) = \frac{\left(S_t^{\,b} - S_0^{\,b}\right) - \left(S_t^{\,n} - S_0^{\,n}\right)}{\left(S_t^{\,b} - S_0^{\,b}\right)} \times 100$$

where S represents the sebum content, n represents the test cream, b represents the blank cream, 0 denotes the baseline time point, and t denotes the measurement time point; a higher value indicates better adsorption performance.

3 Results and discussion

The flower-like mesoporous silica spheres (FLS) were synthesized *via* a bi-phase microemulsion synthetic strategy.[36] As illustrated in Fig. 1a, CTAB was employed as a surfactant in a water–cyclohexane system to form oil–swollen micelles. Upon thermal decomposition of urea at 70 °C, the gradual increase in pH promotes the hydrolysis of TEOS. The resulting siloxane

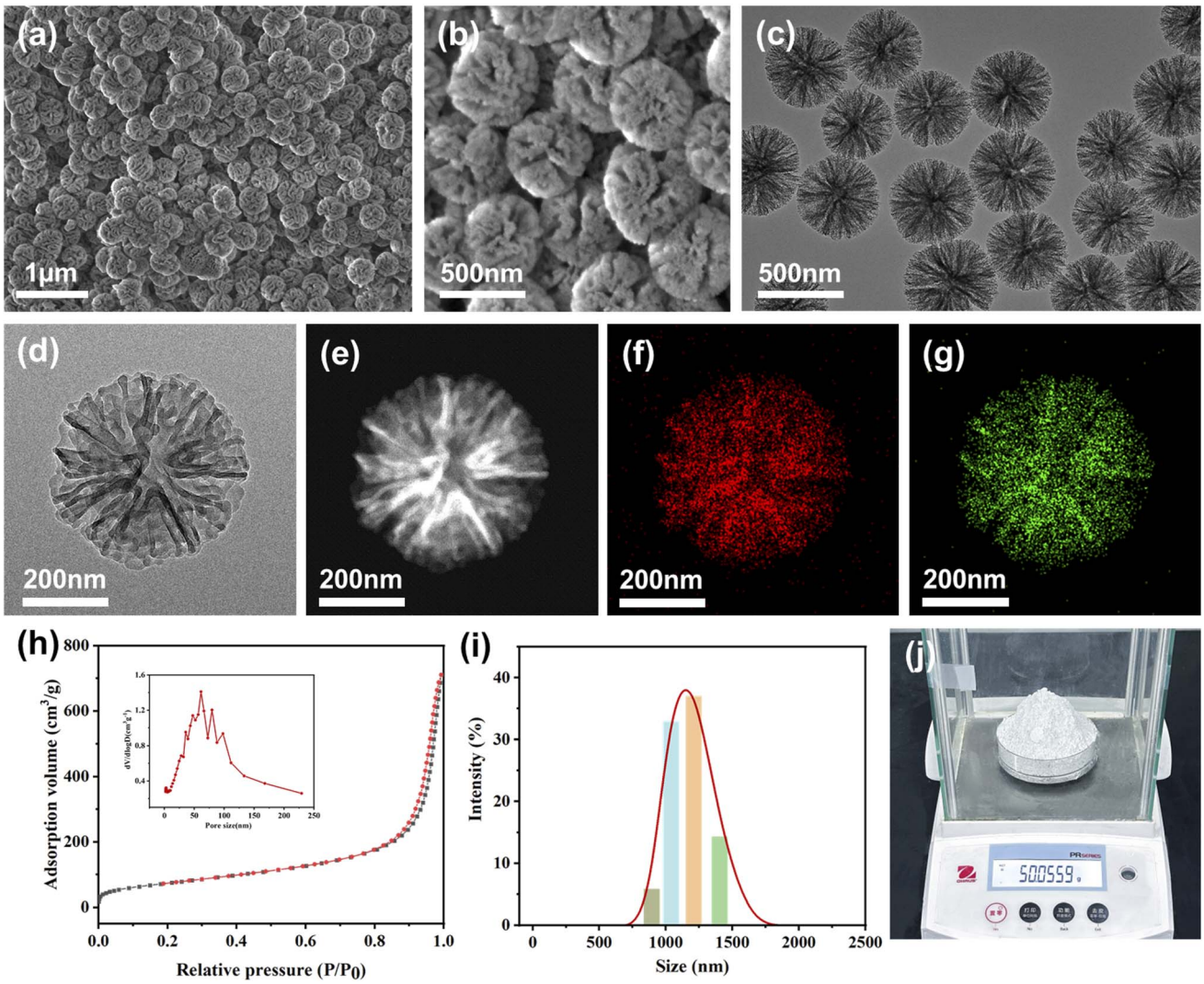

Fig. 2 (a and b) SEM and (c) TEM images of FLS. (d) High-magnification TEM image of a representative FLS nanoparticle. (e–g) HAADF-STEM and EDS mapping images of FLS. (h) N_2 sorption isotherm and the corresponding pore size distribution of FLS. (i) The hydrodynamic diameter of FLS. (j) Photograph of the obtained FLS powder in the large-scale synthesis used in the oil-control cosmetic formulations.

oligomers subsequently co-assemble and cross-link with the cyclohexane–swollen CTAB micelles, leading to the formation of mesostructured silica frameworks. After removal of the organic templates by calcination, mesoporous silica spheres with radially aligned mesoporous channels were obtained.

Notably, in our synthetic system, the presence of cyclohexane plays a role beyond simple micellar swelling. In contrast to the conventional Stöber-derived mesoporous silica, where cylindrical micelles typically act as soft templates,[37] cyclohexane in the biphasic system induces micellar swelling and fusion, which in turn drives the evolution of micellar morphology from conventional cylindrical structures to anisotropic, petal-like assemblies. This dynamic micellar transformation is crucial for the formation of the characteristic flower-like topology observed in the final FLS.

The scanning electron microscopy (SEM) images (Fig. 2a and b) show that the FLS particles exhibit spherical nanostructures with petal-like protrusions, demonstrating a flower-like morphology. The atomic force microscopy (AFM) images (Fig. S1) clearly show that the FLS nanoparticles possess pronounced surface undulations along with abundant nanoscale pits and protrusions, which is consistent with the petal-like topological structure observed by SEM. The low-magnification transmission electron microscopy (TEM) image (Fig. 2c) demonstrates the uniform particle size of monodispersed FLS and reveals the mesoporous structure of FLS with radially ordered mesoporous channels extending from the core towards the surface. Measured from SEM and TEM images, the particle size of the FLS is estimated to be ~370 nm (Fig. S2). Detailed characterization of a single FLS nanoparticle through TEM (Fig. 2d) reveals the large-opening mesoporous channels inside FLS, which connect with petal-like surface corrugations, creating a hierarchical interconnected pore network. The high-angle annular dark field imaging in the scanning TEM (HAADF-STEM) and energy dispersive X-ray spectroscopy (EDS) mapping images show a homogeneous distribution of the Si and O elements in a typical FLS nanoparticle (Fig. 2e–g).

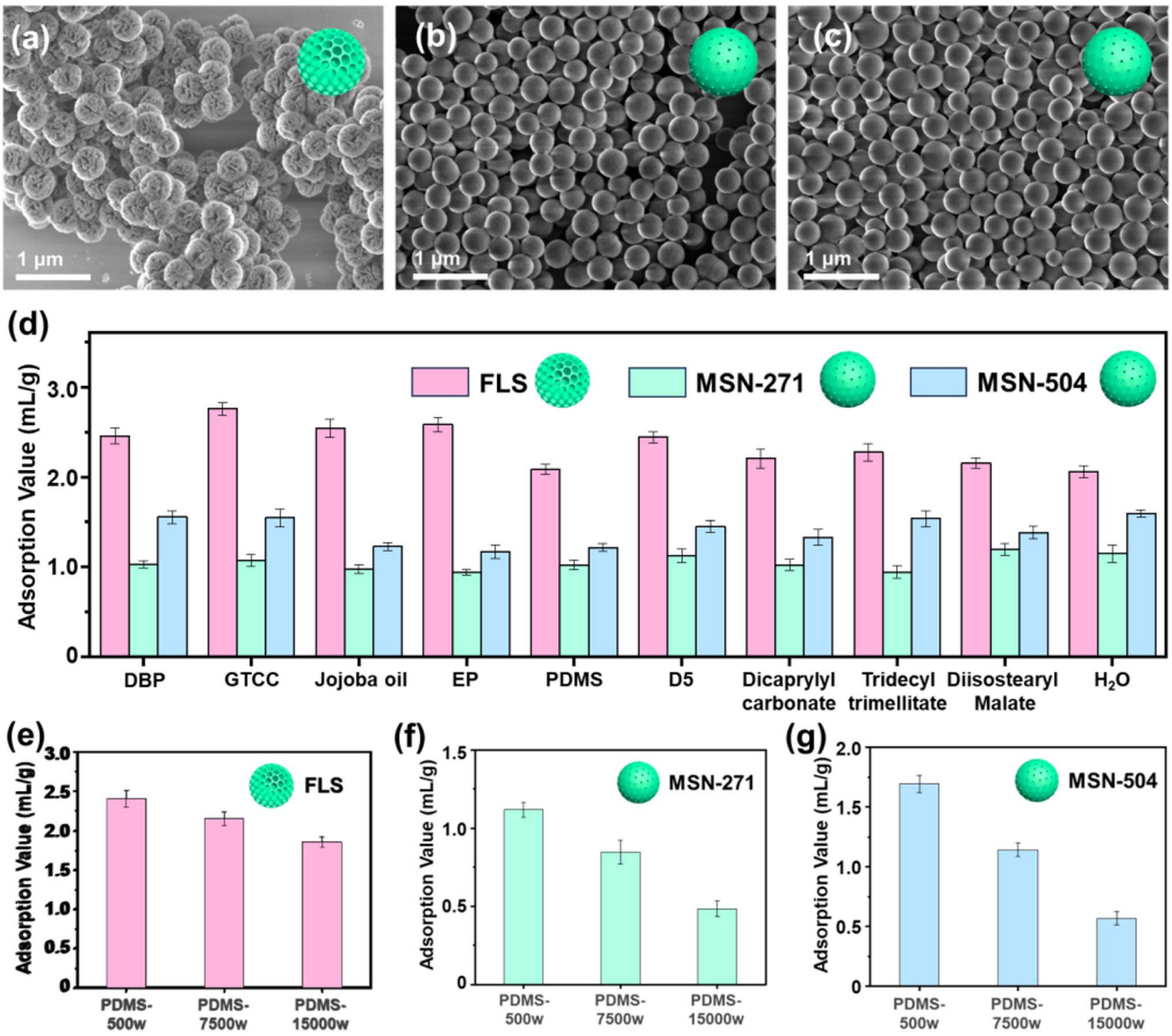

Fig. 3 SEM images of (a) FLS, (b) MSN-271 and (c) MSN-504. (d) The oil absorption capacities of FLS, MSN-271 and MSN-504 across ten commonly used oil molecules. (e–g) The oil absorption capacities of (e) FLS, (f) MSN-271 and (g) MSN-504 for PDMS with different molecular weights.

The N_2 adsorption–desorption isotherm of FLS (Fig. 2h) exhibits a type-IV curve with a distinct H4-type hysteresis loop in the relative pressure (P/P_0) range of 0.8–1.0, characteristic of materials possessing mesoporous structures. The specific surface area, calculated using the Brunauer–Emmett–Teller (BET) method, was approximately 256 $m^2\ g^{-1}$. The pore size distribution was derived from the adsorption branch of the isotherm using the Barrett–Joyner–Halenda (BJH) model, showing a maximum at ~24.4 nm, while the total pore volume, estimated at $P/P_0 \approx 0.99$, was ~1.12 $cm^3\ g^{-1}$. It is noted that the hysteresis loop at high relative pressure may encompass contributions from both the intrinsic radially aligned mesochannels (as confirmed by TEM) and the interparticle voids arising from the flower-like morphology.[38,39] The TGA results (Fig. S3) show that the total weight loss of FLS over the temperature range from 0 to 800 °C is approximately 3.22%. Importantly, dominant weight loss occurs below 150 °C, which can be reasonably attributed to the removal of physically adsorbed water. Beyond this temperature, the mass remains essentially constant, indicating that the FLS framework possesses excellent structural stability at elevated temperatures. Furthermore, there are no discernible weight-loss steps in the temperature range typically associated with CTAB decomposition (250–450 °C), indicating the absence of residual organic surfactant. Fourier-transform infrared spectroscopy (FTIR) (Fig. S4) shows key characteristic peaks of FLS of 1093 cm^{-1} (asymmetric stretching vibration of Si–O–Si), 799 cm^{-1} (symmetric stretching vibration of surface Si–O), and 467 cm^{-1} (bending vibration of Si–O). And the absence of C–H vibration peaks at 958 cm^{-1} confirms the complete removal of CTAB

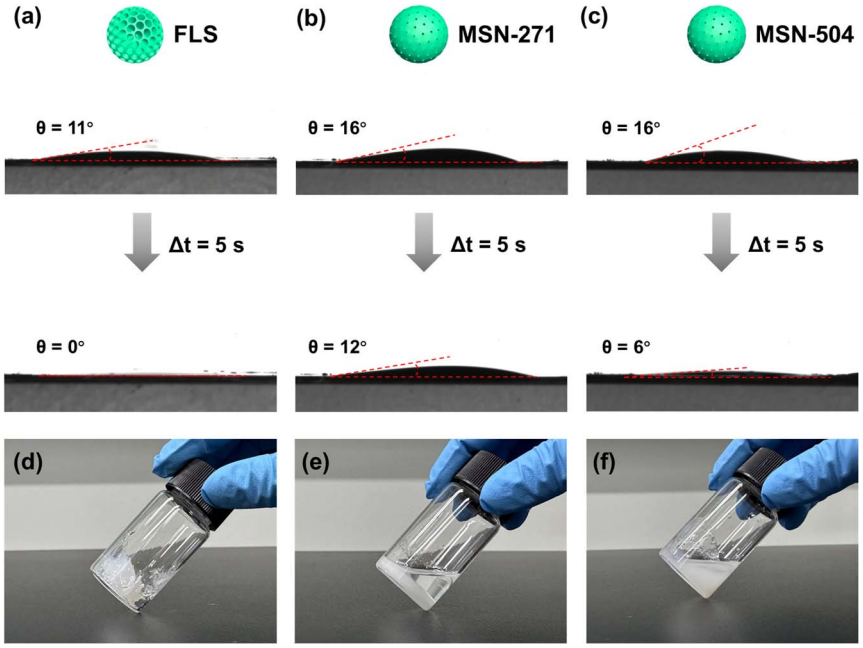

Fig. 4 The initial contact angles and contact angles after 5 seconds of the water droplet on the surface of the samples: (a) FLS, (b) MSN-271 and (c) MSN-504. The photograph of the oil immersion tests with equal masses of materials: (d) FLS, (e) MSN-271 and (f) MSN-504.

template. The zeta potential of FLS is measured to be −39.58 mV (Fig. S5), which can be attributed to abundant surface Si–OH groups. Dynamic light scattering (DLS) measurements in aqueous dispersion yields an average hydrodynamic diameter of ~1200 nm (Fig. 2i), our synthesis strategy enables a robust and scalable preparation of FLS, in which simple proportional magnification allows the laboratory production of tens of grams of samples in a single batch (Fig. 2j). The obtained FLS sample appeared as pristine white powders, which were directly used for oil-adsorption tests and employed in subsequent produce oil-control cosmetic formulations.

To systematically explore the impact of the flower-like structure on oil absorption performance, we tested and compared the oil adsorption capability of FLS with conventional mesoporous silica nanomaterials (MSN). In this work, two kinds of conventional mesoporous silica nanoparticles were synthesized and tested as contrast samples: (1) mesoporous silica

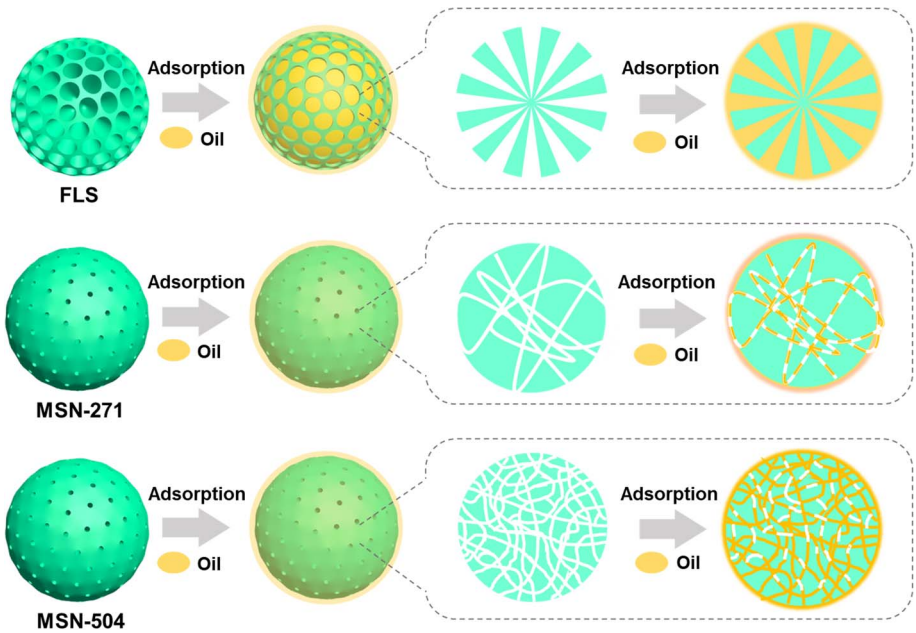

Fig. 5 Schematic illustration of oil adsorption mechanism of FLS, MSN-271 and MSN-504.

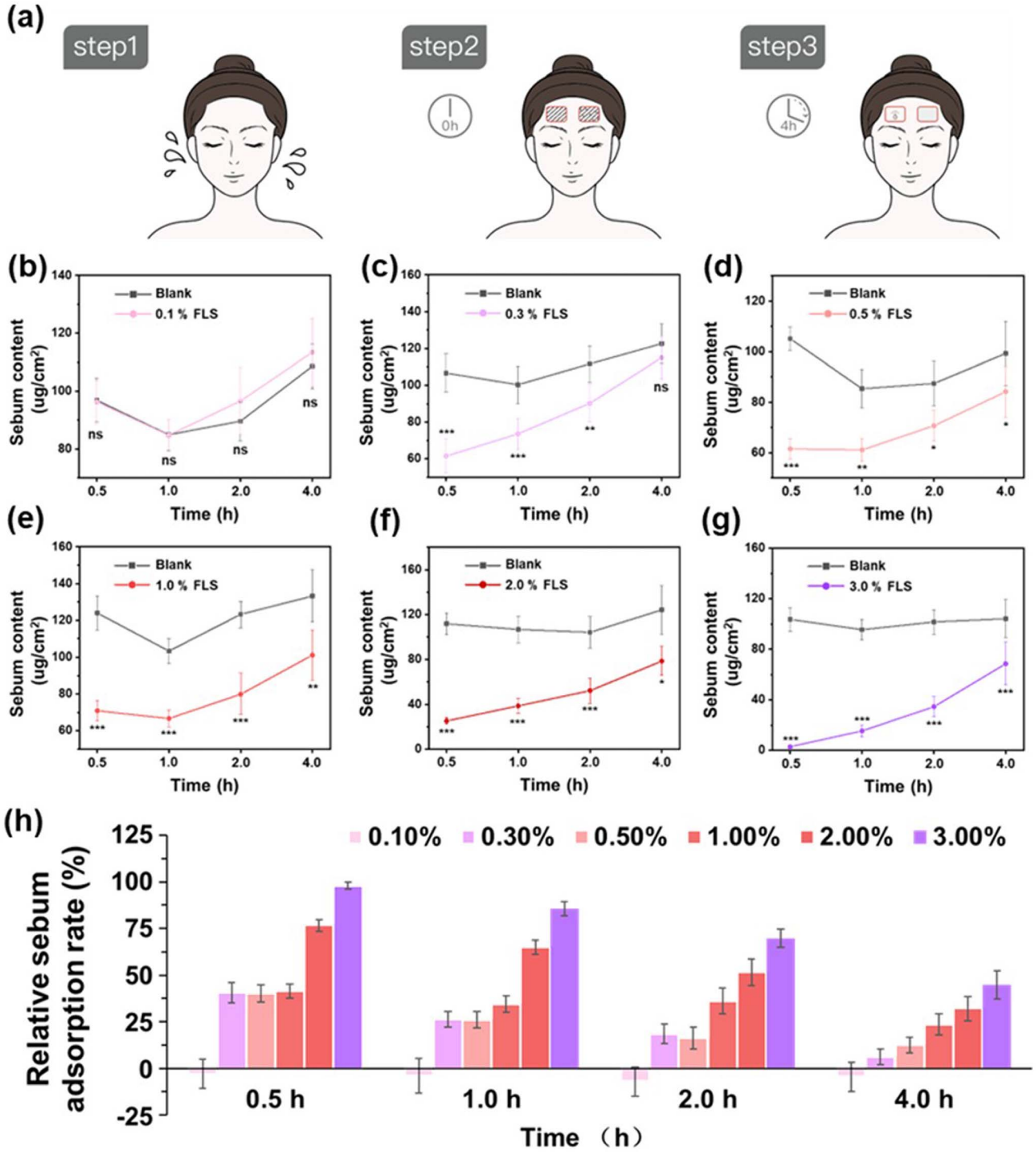

Fig. 6 (a) Schematic illustration of human skin oil control test methodology. Sebum content variation after the post-application of the blank cream and test cream with different addition of FLS: (b) 0.1 wt%; (c) 0.3 wt%; (d) 0.5 wt%; (e) 1.0 wt%; (f) 2.0 wt% and (g) 3.0 wt%. (*p < 0.05, **p < 0.01, ***p < 0.001, nsp > 0.05) (h) Relative sebum adsorption change rate calculated from the above test.

nanospheres with lower specific surface area (~271 m^2 g^{-1}, MSN-271) and (2) with higher surface area (~504 m^2 g^{-1}, MSN-504). Their corresponding pore volumes were 0.55 cm^3 g^{-1} and 0.22 cm^3 g^{-1}, and their average pore sizes were 6 nm and 3 nm, respectively. According to the SEM characterizations (Fig. 3a–c), all three samples possess similar particle size while the morphology of FLS is distinctively different from the MSNs. The TGA results (Fig. S6) show that both MSN samples exhibit thermal stability comparable to that of FLS. Notably, the surface area of MSN-271 is comparable to that of FLS, whereas MSN-504 shows a much larger surface area, far exceeding FLS (Fig. S7). The selection of these three samples not only enables us to

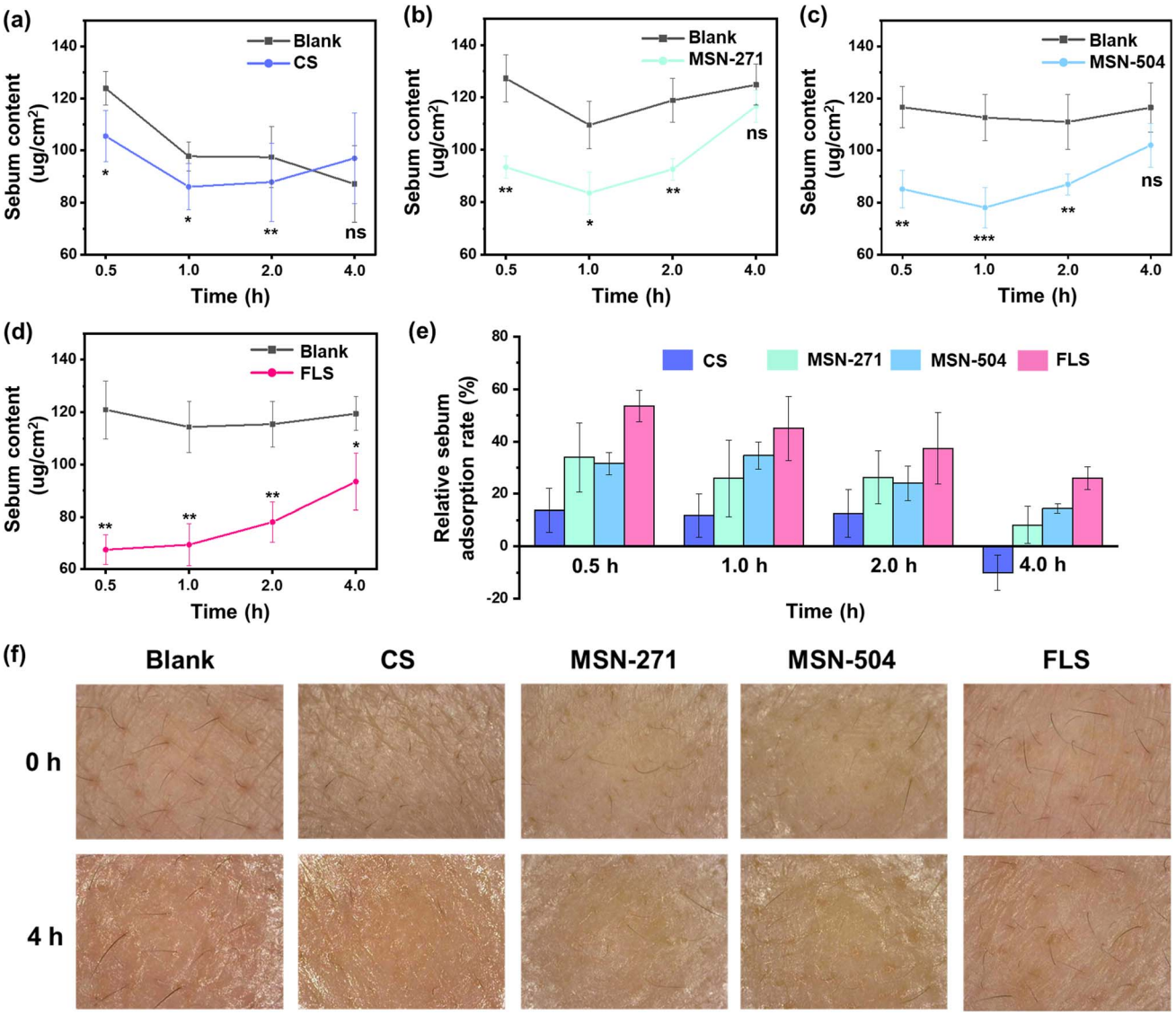

Fig. 7 Sebum content variation after the application of the test creams containing (a) CS, (b) MSN-271, (c) MSN-504 and (d) FLS. (e) Relative sebum adsorption change rate calculated from the above test. (*$p < 0.05$, **$p < 0.01$, ***$p < 0.001$, nsp > 0.05) (f) Photographs of the volunteers' skin after the application of the test creams.

assess the effect of specific surface area on oil absorption performance, but also allows a direct comparison of the role of meso-structural features in governing oil absorption.

Then, the oil absorption capacities of the three samples were evaluated using ten commonly used oil molecules as model to simulate sebum secretion. As shown in Fig. 3d, FLS exhibits the highest absorption value across all test oils, highlighting its superior potential for adsorbing skin sebum secretions. Remarkably, the oil absorption capacity of FLS is twice that of MSN-271 and approximately 1.5 times that of MSN-504. Considering that the surface area of MSN-504 is significantly higher than that of FLS, this superior performance highlights the critical role of the flower-like topology in facilitating efficient oil adsorption. Further investigations revealed the exceptional ability of FLS to absorb oils with large molecular weight (Fig. 3e–g). Specifically, FLS maintained an adsorption capacity of 1.86 mL g^{-1} even for PDMS with a high molecular weight of 15 000 w (PDMS-15 000 w) (Fig. 3e), whereas both MSN-271 and MSN-504 showed a sharp decline in performance with increasing molecular weight (Fig. 3f, and g). For instance, for the PDMS with a lower molecule weight of 500 w (PDMS-500 w), FLS show a high adsorption capacity of 2.41 mL g^{-1}, representing a 42.6% increase over MSN-504 (1.69 mL g^{-1}). More strikingly, for PDMS-15 000 w, FLS achieved a 226.3% enhancement compared to MSN-504 (0.57 mL g^{-1}). These results collectively demonstrate that FLS not only outperforms conventional mesoporous silica in overall oil adsorption but also exhibits a uniquely enhanced capacity for high-molecular-weight oils, underscoring the pivotal contribution of its flower-like mesostructure.

To explore the mechanism underlying the enhanced oil absorption capacity of FLS, we conducted contact angle and oil

immersion tests on the three silica samples. As shown in Fig. 4a–c, all the samples display comparable hydrophilic surface property, with the contact angle ranging from 10° to 20°. Notably, the contact angle of FLS decreased from 11° to 0° within 5 seconds (rate: 2.2° s^{-1}), which was notably faster than that observed for MSN-504 (from 16° to 6°, rate: 2.0° s^{-1}) and MSN-271 (from 16° to 12°, rate: 0.8° s^{-1}). This fast wetting behavior indicates excellent surface wettability of FLS and suggests that the hierarchical flower-like topology effectively facilitates capillary-driven liquid infiltration into the mesoporous channels, thereby contributing to its superior oil-adsorption performance.

Furthermore, in oil immersion tests where equal masses of materials were exposed to identical volume of DBP, the three samples exhibited markedly different performances (Fig. 4d–f). After oil immersion, FLS appeared solidified with neglectable free oil, indicating a complete oil absorption. In contrast, the MSN-271 presented clear solid–liquid phase separation with large amount of free oil, indicating a minimal oil adsorption capability. While the MSN-504 sample performed better than the MSN-271 but still retained substantial free oil after immersion, reflecting the inadequate oil adsorption capability of conventional MSN. These results run counter to theoretical expectations, as MSN-504, with its higher porosity and large specific surface area compared to FLS, would be expected to accommodate more oil molecules. The discrepancy underscores the critical role of pore nanoarchitecture in enabling efficient pore volume utilization and maximizing oil adsorption capacity. Taking advantage of the unique flower-like morphology, FLS provide highly accessible pathways for oil molecules through large opening mesoporous channels. Once entering the structure, oil molecules can readily migrate along the depth of the radially oriented channels, effectively avoiding the pore blockage commonly encountered in the smaller and disordered pore networks of conventional MSNs, thereby facilitating efficient penetration and full utilization of the internal pore spaces of FLS.

Based on the above findings, we propose a topology-mediated oil penetration mechanism to account for the superior oil absorption capacity of FLS (Fig. 5). In general, the oil fills the mesoporous structures through the following steps: (1) initial contact with entrance of the pores on the surface, (2) transport through pore openings and (3) penetration into the inner regions of the particles until saturation. In the case of FLS, the radially arranged nano-petals generate large concave surface features (as confirmed by SEM and AFM characterization), providing highly accessible entry points for instantaneous oil uptake. Once entering, oil molecules are efficiently guided along the straight, radially oriented mesoporous channels towards the particle center, ensuring complete saturation and maximizing pore volume utilization. In contrast, the surface cavities of MSN-271 and MSN-504 are much smaller, which hinders initial oil access. Moreover, their worm-like mesoporous structure significantly slow down penetration kinetics, as reflected in the slower wetting rates observed in the contact angle experiments (Fig. 3a–c). More critically, unlike the radially oriented mesoporous channels in FLS, the disordered pore networks of these conventional MSNs restrict full accessibility to internal void spaces, resulting in incomplete pore filling and reduced oil adsorption capacity. It is also worth emphasizing that compared with the disordered mesoporous structures of MSNs, the unique combination of large surface concavities and radially oriented mesoporous channels in FLS offers distinct advantages for accommodating large-molecule oils. Therefore, despite having a comparable surface area (MSN-271) or even a much higher one (MSN-504) relative to FLS (256 m^2 g^{-1}), both conventional MSNs exhibit markedly inferior oil adsorption capacity. The significant improvement achieved by FLS highlights the decisive role of topological design in enhancing oil adsorption and underscores its potential in the development of next-generation oil-control materials and cosmetic formulations.

The sebum adsorption performance of FLS was further evaluated by using the standard human skin oil control methodology (Fig. 6a). Volunteers' faces were thoroughly cleansed, followed by a 30-minute acclimatization period before measuring baseline sebum content on both forehead sides. Then, after the post-application of the blank cream (without FLS) and the test cream (with FLS) at 0.5, 1.0, 2.0, and 4.0-hours, the sebum content was measured and calculated based on the baseline sebum content. The FLS exhibits a clear dose-dependent oil-control effect. Initially, with an addition of 0.1 wt%, the sebum content values of the test cream were nearly the same as the blank group throughout the test (Fig. 6b). When the addition of FLS increased to 0.3 wt% (Fig. 6c), an apparent oil-control performance can be clearly observed in 2 hours while such ability cannot be maintained to 4 hours. After the further increased addition of 0.5 wt% and above (Fig. 6d–g), the test cream with FLS show distinctive sebum adsorption capacity with prolonged time period to 4 hours. The relative sebum adsorption change rate of the test cream with different concentration of FLS was calculated to quantitatively evaluate the oil adsorption performance (Fig. 6h). Throughout the observation period (0.5 h to 4.0 h), FLS not only exhibited immediate sebum adsorption but also demonstrated prolonged oil-control efficacy with appropriate addition amount in the cream. With an FLS addition of 3.0 wt%, the test cream exhibited a significant relative sebum adsorption change rate of 97.9% at 0.5 h and maintained a high level of 44.6% at 4.0 h.

To further assess the oil absorption performance of FLS in cosmetic oil-control applications, comparative studies were conducted against MSN-271, MSN-504, and one commonly used commercial cosmetic silica (CS). All materials were incorporated into the same formulation base at an equivalent addition of 1.0 wt%. Using a double-blind design, 20 healthy volunteers were recruited for longitudinal observations over a 4-hour period (Fig. 7a–d). During the test, CS exhibited only weak oil-control capability within 0.5 h. While MSN-271 and MSN-504 demonstrated comparatively better oil control than CS, their performance declined significantly by 4 h. Quantitative analysis *via* relative sebum adsorption change rate (Fig. 7e) revealed that FLS achieved 53.5% at 0.5 h, which is 3.9-fold higher than CS (13.7%) and 1.7-fold higher than MSN-504 (31.5%). More importantly, FLS maintained 26.0% efficacy at 4.0 h, 1.8-fold higher than MSN-504 (14.5%). Visual observations of the volunteers' skin further confirmed that FLS provided the most effective sebum gloss suppression (Fig. 7f). Collectively, these

findings not only validate the exceptional sebum adsorption capability of FLS in the human skin environment but also provide compelling experimental evidence for its potential application in cosmetic formulations.

4 Conclusions

In summary, we have successfully synthesized flower-like mesoporous silica spheres (FLS) featuring topology-enhanced oil adsorption capability for cosmetic oil-control applications. Comprehensive characterizations revealed that FLS possessed a petal-like surface topology and hierarchical interconnected pore network with radially oriented meschannels (surface area: 256 m^2 g^{-1}, pore size: 24.4 nm, pore volume: 1.12 cm^3 g^{-1}). Notably, FLS exhibited superior oil absorption capacity, achieving up to twofold higher capacity than conventional MSN across a broad range of commonly used test oils. Its advantage was particularly pronounced for high-viscosity large molecules like PDMS-15000 w (1.86 mL g^{-1}, +226.3% *vs.* MSN). The enhanced oil adsorption is attributed to a unique topology-mediated oil penetration mechanism, wherein the large concave surface structures of FLS provide highly accessible entry sites for rapid oil uptake, while the radially aligned mesopores facilitate efficient oil transport and maximize pore utilization. *In vivo* human skin studies further confirmed the superior cosmetic efficacy of FLS. Even at a low addition level (0.3 wt%), FLS maintained oil-control activity for up to 4 h, showing dose-dependent enhancement in sebum adsorption. In controlled, double-blind comparative trials, FLS outperformed both commercial silica and conventional MSN, achieving significantly superior oil absorption and sebum gloss suppression throughout the 4-hour observation window. Collectively, this work establishes FLS as an advanced oil-control material, underscoring the importance of surface topological engineering in designing advanced mesoporous adsorbents for cosmetic and related applications.

Author contributions

M. Y., W. W., Y. Y. and X. L. designed and coordinated this study and reviewed the manuscript. M. Y., Z. Z. Y. W. and W. W. conducted the experiments and analyzed the data. M. Y. W. W. and X. L. contributed to the experimental design, data interpretation, and manuscript writing. Q. L. and D. Z. provided guidance for this study. All authors have read and approved the final version of the manuscript.

Conflicts of interest

The authors declare no conflicts of interest.

Data availability

All the data that support the findings of this study are available in the text of this article.

Supplementary information (SI) is available. See DOI: https://doi.org/10.1039/d5ra08525j.

Acknowledgements

This work was supported by the Science and Technology Commission of Shanghai (24ZR1405900), National Natural Science Foundation of China (22525501, 22475049, 82103694, 22088101); the Key Basic Research Program of Science and Technology Commission of Shanghai Municipality (22JC1410200), the Shanghai Pilot Program for Basic Research-Fudan University (22TQ004), Science and Technology Commission of Shanghai Municipality (2024ZDSYS02, 25PY2600100).

References

1 A. G. Slater and A. I. Cooper, Porous materials. Function-led design of new porous materials, *Science*, 2015, **348**(6238), aaa8075.
2 R. L. Siegelman, E. J. Kim and J. R. Long, Porous materials for carbon dioxide separations, *Nat. Mater.*, 2021, **20**(8), 1060–1072.
3 T. D. Bennett, F. X. Coudert, S. L. James and A. I. Cooper, The changing state of porous materials, *Nat. Mater.*, 2021, **20**(9), 1179–1187.
4 H. Wang, Y. Shao, S. Mei, Y. Lu, M. Zhang, J. K. Sun, K. Matyjaszewski, M. Antonietti and J. Yuan, Polymer-derived heteroatom-doped porous carbon materials, *Chem. Rev.*, 2020, **120**(17), 9363–9419.
5 S. Das, P. Heasman, T. Ben and S. Qiu, Porous organic materials: strategic design and structure–function correlation, *Chem. Rev.*, 2017, **117**(3), 1515–1563.
6 W. Li, J. Liu and D. Zhao, Mesoporous materials for energy conversion and storage devices, *Nat. Rev. Mater.*, 2016, **1**(6), 1–7.
7 L. Duan, C. Wang, W. Zhang, B. Ma, Y. Deng, W. Li and D. Zhao, Interfacial assembly and applications of functional mesoporous materials, *Chem. Rev.*, 2021, **121**(23), 14349–14429.
8 D. Zhao, J. Feng, Q. Huo, N. Melosh, G. H. Fredrickson, B. F. Chmelka and G. D. Stucky, Triblock copolymer syntheses of mesoporous silica with periodic 50 to 300 angstrom pores, *Science*, 1998, **279**(5350), 548–552.
9 Y. Li and J. Shi, Hollow-structured mesoporous materials: chemical synthesis, functionalization and applications, *Adv. Mater.*, 2014, **26**(20), 3176–3205.
10 M. Vallet-Regí, F. Balas and D. Arcos, Mesoporous materials for drug delivery, *Angew. Chem., Int. Ed.*, 2007, **46**(40), 7548–7558.
11 C. H. Lee, T. S. Lin and C. Y. Mou, Mesoporous materials for encapsulating enzymes, *Nano today*, 2009, **4**(2), 165–179.
12 M. Manzano and M. Vallet-Regí, Mesoporous silica nanoparticles for drug delivery, *Adv. Funct. Mater.*, 2020, **30**(2), 1902634.
13 Y. Chen, H. Chen and J. Shi, In vivo bio-safety evaluations and diagnostic/therapeutic applications of chemically designed mesoporous silica nanoparticles, *Adv. Mater.*, 2013, **25**(23), 3144–3176.

14 H. C. Wang, S. Y. Lin, A. C. Tang, B. P. Singh, H. C. Tong, C. Y. Chen, Y. C. Lee, T. L. Tsai and R. S. Liu, Mesoporous Silica Particles Integrated with AllInorganic CsPbBr3 Perovskite Quantum-DotNanocomposites (MP-PQDs) with High Stability and Wide Color Gamut Used for Backlight Display, *Angew. Chem., Int. Ed.*, 2016, **55**, 7924–7929.

15 Z. Li, J. C. Barnes, A. Bosoy, J. F. Stoddart and J. I. Zink, Mesoporous silica nanoparticles in biomedical applications, *Chem. Soc. Rev.*, 2012, **41**(7), 2590–2605.

16 C. Xu, M. H. Yu, O. Noonan, J. Zhang, H. Song, H. W. Zhang, C. Lei, Y. T. Niu, X. D. Huang, Y. N. Yang and C. Z. Yu, Core-cone structured monodispersed mesoporous silica nanoparticles with ultra-large cavity for protein delivery, *Small*, 2015, **11**(44), 5949–5955.

17 W. X. Wang, P. Y. Wang, X. . T. Tang, A. A. Elzatahry, S. W. Wang, D. Al-Dahyan, M. Y. Zhao, C. Yao, C. T. Hung, X. H. Zhu, T. C. Zhao, X. M. Li, F. Zhang and D. Y. Zhao, Facile synthesis of uniform virus-like mesoporous silica nanoparticles for enhanced cellular internalization, *ACS Cent. Sci.*, 2017, **3**(8), 839–846.

18 Y. Z. Ma, H. J. Zhang, R. F. Lin, Y. Ai, K. Lan, L. L. Duan, W. Y. Chen, X. Z. Duan, B. Ma, C. Y. Wang, X. M. Li and D. Y. Zhao, Remodeling nanodroplets into hierarchical mesoporous silica nanoreactors with multiple chambers, *Nat. Commun.*, 2022, **13**(1), 6136.

19 X. R. Huang, T. T. Ren, R. F. Lin, Z. R. Lv, S. X. Yin, Y. F. Xu, Y. P. Liu, C. T. Hung, M. Wang, X. M. Li, T. C. Zhao and D. Y. Zhao, Stepwise Self-Assembly of Multisegment Mesoporous Silica Nanobamboos for Enhanced Thermal Insulation, *J. Am. Chem. Soc.*, 2025, **147**(18), 15890–15900.

20 P. Verma, Y. Kuwahara, K. Mori, R. Raja and H. Yamashita, Functionalized mesoporous SBA-15 silica: recent trends and catalytic applications, *Nanoscale*, 2020, **12**(21), 11333–11363.

21 S. Luebberding, N. Krueger and M. Kerscher, Skin physiology in men and women: in vivo evaluation of 300 people including TEWL, SC hydration, sebum content and skin surface pH, *Int. J. Cosmet. Sci.*, 2013, **35**(5), 477–483.

22 O. Sonneville-Aubrun, J. T. Simonnet and F. L'alloret, Nanoemulsions: a new vehicle for skincare products, *Adv. Colloid Interface Sci.*, 2004, **108**, 145–149.

23 B. Y. Kim, J. W. Choi, K. C. Park and S. W. Youn, Sebum, acne, skin elasticity, and gender difference–which is the major influencing factor for facial pores?, *Sking Res. Technol.*, 2013, **19**(1), e45–e53.

24 P. Lozada, L. Victoria-Tinoco, A. M. Muñoz and J. Rojas, Evaluation of Sebum Control and Safety for Daily Use of a Cosmetic Elastomer Formulated with Vegetable Oils from Peruvian Biodiversity, *Cosmetics*, 2025, **12**(2), 66.

25 A. Pura, I. Dusenkova and J. Malers, Adsorption of organic compounds found in human sebum on latvian illitic, kaolinitic, and chloritic phyllosilicates, *Clays Clay Miner.*, 2014, **62**(6), 500–507.

26 J. R. Costa, T. Neto, S. S. Pedrosa, S. C. Sousa, J. Azevedo-Silva, D. Tavares-Valente, A. Mendes, M. E. Pintado, J. C. Fernandes, A. S. Oliveira and A. R. Madureira, Biogenic silica microparticles as a new and sustainable cosmetic ingredient: Assessment of performance and quality parameters, *Colloids Surf., B*, 2023, **226**, 113305.

27 M. J. Hong, Y. Lee, S. J. Kyung, J. Choi and H. J. Lee, Sustainable and durable color cosmetics: Riboflavin phosphate-mediated photo-crosslinked casein films with tannic acid, *Biomater. Sci.*, 2024, **12**(23), 6136–6147.

28 H. S. Lee, D. K. Sung, S. H. Kim, W. I. Choi, E. T. Hwang, D. J. Choi and J. H. Chang, Controlled release of astaxanthin from nanoporous silicified-phospholipids assembled boron nitride complex for cosmetic applications, *Appl. Surf. Sci.*, 2017, **424**, 15–19.

29 Q. Fu, F. Ansari, Q. Zhou and L. A. Berglund, Wood nanotechnology for strong, mesoporous, and hydrophobic biocomposites for selective separation of oil/water mixtures, *ACS Nano*, 2018, **12**, 2222–2230.

30 Y. Ahn and S. Y. Kwak, Functional mesoporous silica with controlled pore size for selective adsorption of free fatty acid and chlorophyll, *Microporous Mesoporous Mater.*, 2020, **306**, 110410.

31 B. Sedai, J. L. Zhou, N. Fakhri, A. Sayari and R. T. Baker, Solid Phase Extraction of Bio-Oil Model Compounds and LigninDerived Bio-Oil Using Amine-Functionalized Mesoporous Silicas, *ACS Sustainable Chem. Eng.*, 2018, **6**, 9716–9724.

32 W. Zhang, S. Li, J. Zhang, Z. Zhang and F. Dang, Synthesis and adsorption behavior study of magnetic fibrous mesoporous silica, *Microporous Mesoporous Mater.*, 2019, **282**, 15–21.

33 Z. D. Shao, Q. J. Zhang, Y. M. Zheng and X. Cheng, A novel pearls-like hierarchical porous silica aerogel monolith for efficient oil/water separation, *J. Porous Mater.*, 2024, **31**(3), 843–853.

34 J. Ma, Q. Liu, D. Chen, S. Wen and T. Wang, CO2 adsorption on amine-modified mesoporous silicas, *J. Porous Mater.*, 2014, **21**(5), 859–867.

35 L. X. Zhang, M. Zhu, L. M. Guo, L. Li and J. L. Shi, Bilirubin adsorption property of mesoporous silica and amine-grafted mesoporous silica, *Nano-Micro Lett.*, 2009, **1**(1), 14–18.

36 D. K. Shen, J. P. Yang, X. M. Li, L. Zhou, R. Y. Zhang, W. Li, L. Chen, R. Wang, F. Zhang and D. Y. Zhao, Biphase stratification approach to three-dimensional dendritic biodegradable mesoporous silica nanospheres, *Nano Lett.*, 2014, **14**(2), 923–932.

37 W. Stober, A. Fink and E. Bohn, Controlled growth of monodisperse silica spheres in the micron size range, *J. Colloid Interface Sci.*, 1968, **26**, 62–69.

38 C. Amgoth, Y. H. He and S. P. Wang, Metal (Au)-decorated chitosan-L-arginine polymeric vector for codelivery of gefitinib and miR125b for lung cancer therapy, *ACS Appl. Polym. Mater.*, 2022, **4**(3), 1675–1687.

39 C. Amgoth, S. J. D. S. Doddapaneni and G. Dharmapuri, Self-assembled block copolymer [(BenzA)-b-(PCL)] micelles to orient randomly distributed AuNPs into hollow core-shell morphology and its role as payload for nanomedicines, *Mater. Sci. Eng., C*, 2018, **92**, 790–799.